Electronic structure of the titanium-based oxypnictide superconductor Ba_{0.95}Na_{0.05}Ti_{2}Sb_{2}O and direct observation of its charge density wave order

Q. Song, Y. J. Yan, Z. R. Ye, M. Q. Ren, D. F. Xu, S. Y. Tan, X. H. Niu, B. P. Xie, T. Zhang, R. Peng, H. C. Xu, J. Jiang, and D. L. Feng

Phys. Rev. B **93**, 024508 — Published 11 January 2016

DOI: 10.1103/PhysRevB.93.024508

Electronic structure of the titanium-based oxypnictide superconductor $Ba_{0.95}Na_{0.05}Ti_2Sb_2O$ and direct observation of its charge density wave order

Q. Song, Y. J. Yan, Z. R. Ye, M. Q. Ren, D. F. Xu, S. Y. Tan, X. H. Niu, B. P. Xie, T. Zhang, R. Peng, H. C. Xu, J. Jiang,* and D. L. Feng†
State Key Laboratory of Surface Physics, Department of Physics, and Advanced Materials Laboratory, Fudan University, Shanghai 200433, People's Republic of China
(Dated: December 23, 2015)

$Ba_{0.95}Na_{0.05}Ti_2Sb_2O$ is a titanium-based oxypnictide superconductor with possible density wave order. We have performed high resolution angle-resolved photoemission spectroscopy (ARPES) and scanning tunneling microscopy (STM) studies on $Ba_{0.95}Na_{0.05}Ti_2Sb_2O$. Our STM studies find a charge density wave (CDW) order with the wavevector of (π, π). The electronic structure shows both multi-orbital and three-dimensional nature, consistent with the theoretical calculations. The observed Fermi surfaces are well nested along the (π, π) direction, which might drive the CDW transition. Likely due to the weak strength of the CDW order, we do not observe a leading-edge gap. Instead, we observe an overall spectral weight enhancement with decreasing temperature, but the rate of this enhancement is abruptly reduced or diminished in the CDW state, suggesting the suppression of spectral weight or opening of a partial CDW gap. Our results give a comprehensive picture of the electronic structure and direct observation of the CDW order in $Ba_{0.95}Na_{0.05}Ti_2Sb_2O$.

PACS numbers: 71.45.Lr, 74.70.-b, 68.37.Ef, 79.60.-i

I. INTRODUCTION

Layered transition-metal compounds have proven a fruitful stage for novel superconductivity. Intriguingly in these systems, unconventional superconductivity usually emerges in proximity to a spin-ordered or charge-ordered state, for example, in cuprates, iron-based superconductors and layered chalcogenides [1–3]. This offers a clue about searching for unconventional superconductivity in layered compounds. The titanium pnictide oxides, such as $Na_2Ti_2Pn_2O$ and $BaTi_2Pn_2O$ (Pn = As, Sb), are layered systems with distinct transport anomalies that are associated with the formation of density wave order. The transition temperatures are 330 K for $Na_2Ti_2As_2O$, 200 K for $BaTi_2As_2O$, 115 K for $Na_2Ti_2Sb_2O$ and 45 K for $BaTi_2Sb_2O$, respectively[4–6]. So far, the exact nature of the density wave is still unknown, although no sign of spin density wave (SDW) have been found, there is also no direct evidence for a charge density wave (CDW) ground state. Nevertheless, they have been proposed as a candidate parent phase for superconductivity. Many attempts to induce superconductivity in both $Na_2Ti_2Pn_2O$ and $BaTi_2As_2O$ by chemical substitution or Li intercalation have failed, although the temperature of CDW/SDW transition has been successfully suppressed[5].

Superconductivity emerges at 1 K in $BaTi_2Sb_2O$ [7], and a maximal T_c of 5.5 K has been achieved in $Ba_{1-x}Na_xTi_2Sb_2O$ [8]. These make them the only known titanium-pnictide-oxide superconductors. First principles calculations of $BaTi_2Sb_2O$ suggest that the density wave transition is caused by a magnetic instability associated with Fermi surface nesting, and the superconductivity is mediated by spin fluctuations [9]. However, another calculation indicates that a CDW instability may dominate, with the superconductivity driven by conventional electron-phonon interactions in this compound [10]. Experimentally, muon spin rotation (μSR) studies have not found any sign of magnetic order, while a nuclear magnetic resonance (NMR) observed broken in-plane four-fold symmetry at the Sb site without the presence of an internal field [11, 12]. Therefore, CDW order is more likely although no direct evi-

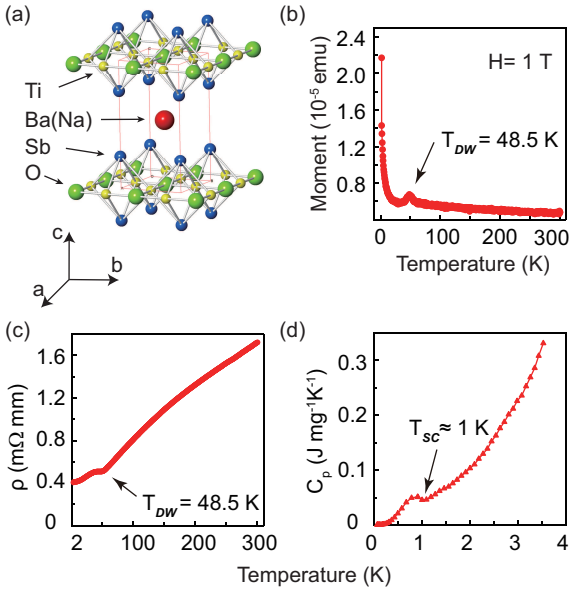

FIG. 1: (Color online) (a) Crystal structure of $Ba_{1-x}Na_xTi_2Sb_2O$. (b) Magnetic susceptibility of $Ba_{0.95}Na_{0.05}Ti_2Sb_2O$ as a function of temperature measured under 1 T, where the anomaly temperature T_{DW} around 48.5 K is taken to indicate the onset of a density wave order. (c) Resistivity measured down to 2 K, which also shows an anomaly at 48.5 K. (d) Low temperature heat capacity down to 50 mK, where the onset of the peak indicates a superconducting transition around 1 K.

*Electronic address: jjiangcindy@gmail.com
†Electronic address: dlfeng@fudan.edu.cn

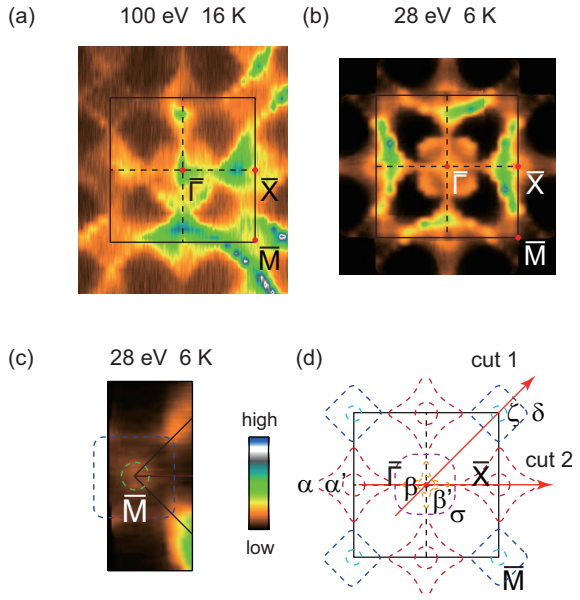

FIG. 2: (Color online) (a) Photoemission intensity map taken with circularly polarized 100 eV photons at 16 K. The intensity was integrated over the energy window of [E_F-10 meV, E_F+10 meV]. $\overline{\Gamma}$, $\overline{M}$ and $\overline{X}$ stand for the high-symmetry points of the projected two-dimensional Brillioun zone (BZ). Data were taken at the SLS. (b) Photoemission intensity map taken with circularly polarized 28 eV photons at 6 K at the SSRL, integrated over the energy window of [E_F-10 meV, E_F+10 meV]. (c) Magnified photoemission intensity map around $\overline{M}$ in panel (b). (d) A schematic of the Fermi surface sheets obtained by tracking the Fermi crossings in panels (a) and (b). As discussed below, the data taken with 100 eV photons are close to the $k_z = 6.8\ 2\pi/c$ plane, and those taken with 28 eV photons are close to the $k_z = 4.5\ 2\pi/c$ plane.

dence has been reported. Meanwhile, the heat capacity data support BCS-like superconductivity in proximity to a CDW instability [13].

To understand why superconductivity should occur in $Ba_{1-x}Na_xTi_2Sb_2O$ among all the known titanium pnictide oxides, and to elucidate the nature of its density wave, it is crucial to study its electronic structure. A previous angle-resolved photoemission spectroscopy (ARPES) study on the density wave state of $BaTi_2As_2O$ has observed anomalous temperature-dependent spectral weight redistribution and partial gap opening at the Fermi patches, which is a region of the Brillouin zone (BZ) with finite spectral weight at the Fermi energy [6]. Later on, ARPES study on $Na_2Ti_2Sb_2O$ did observe a large density wave energy gap at about 65 meV at 7 K [14]. However, till now the electronic structure of the superconducting $Ba_{1-x}Na_xTi_2Sb_2O$ has not been reported.

Here, by performing high resolution ARPES and scanning tunneling microscopy (STM) experiments on high quality single crystals, we studied the three dimensional (3D) electronic structure of $Ba_{0.95}Na_{0.05}Ti_2Sb_2O$. We observed a 3D electron pocket with strong k_z dependence and a quasi-two-dimensional electron pocket around the BZ center, $\overline{\Gamma}$; a quasi-two-dimensional electron pocket and a quasi-two-dimensional hole pocket around the BZ corner, $\overline{M}$; and a 3D hole pocket around the BZ boundary, $\overline{X}$. The low-lying states are contributed by Ti $d_{x^2-y^2}$, d_{xy} and d_{z^2} orbitals. The Fermi surface is well nested along the (π, π) direction. Although we do not observe a leading-edge gap in the density wave state, we find an overall spectral weight enhancement with decreasing temperature, and the rate of this enhancement is abruptly reduced or diminished below the density wave transition temperature. Furthermore, our STM studies have directly observed a CDW order with wavevector of (π, π), consistent with the nesting wavevector observed by ARPES. Of particular note, our results indicate that the CDW strength in $Ba_{1-x}Na_xTi_2Sb_2O$ is weaker than in $BaTi_2As_2O$ or $Na_2Ti_2Sb_2O$, which may be the reason for the emergence of superconductivity here.

II. EXPERIMENTAL

High quality $Ba_{0.95}Na_{0.05}Ti_2Sb_2O$ single crystals were grown by a BaSb self-flux method. Ba pieces and Sb powder were mixed together, heated to 800 °C, and kept for 10 hours. Optimally doped polycrystalline $Ba_{0.75}Na_{0.25}Ti_2Sb_2O$ polycrystals was synthesized with a superconducting transition temperature at 5.5 K from magnetic susceptibility measurements, following the growth recipe in Ref. 8. The powder was then mixed with BaSb flux in a ratio of 1:3. The mixture was loaded into an alumina crucible and then sealed in an iron crucible under Ar environment. It was preheated to 800 °C for 10 hours, then heated to 1350 °C for 5 hours, and finally slowly cooled to 1000 °C at a rate of 3 °C / hour before shutting off the power. Shiny single crystals could be found inside of the containing material. The composition of the single crystals was $Ba_{0.95}Na_{0.05}Ti_2Sb_2O$ based on x-ray diffraction (XRD) measurements, different from the starting polycrystalline material.

The crystal structure of $Ba_{0.95}Na_{0.05}Ti_2Sb_2O$ is shown in Fig. 1(a). The Ti, Sb, and O atoms formed Ti_2Sb_2O octahedron are stacked alternatively with layers of Ba/Na atoms along the c axis. Figures 1(b) and 1(c) show the magnetic susceptibility and resistivity data of $Ba_{0.95}Na_{0.05}Ti_2Sb_2O$, both of which exhibit an anomaly at 48.5 K, indicating a density wave transition. The heat capacity of the $Ba_{0.95}Na_{0.05}Ti_2Sb_2O$ single crystal in Fig. 1(d) shows a superconducting transition around 1 K.

ARPES experiments were performed at the SIS beamline of Swiss Light Source (SLS), beamline 5-4 of Stanford Synchrotron Radiation Lightsource (SSRL) and beamline I05-ARPES of Diamond light source (DLS), all equipped with a Scienta R4000 electron analyzer. The angular resolution was 0.3° and the overall energy resolution was about 7 meV at the SSRL, 10 meV at the DLS and above 10 meV at the SLS depending on different photon energies. The samples were cleaved *in-situ* along the (001) plane and measured under ultra-high vacuum below 9×10^{-11} torr.

STM measurements were performed in a cryogenic STM system at 4.5 K. Platinum tips were used after treatment on Au surface. Topographic images were taken with constant current mode with the bias voltage applied to the sample. The tunneling conductance (dI/dV) was collected by standard lock-in

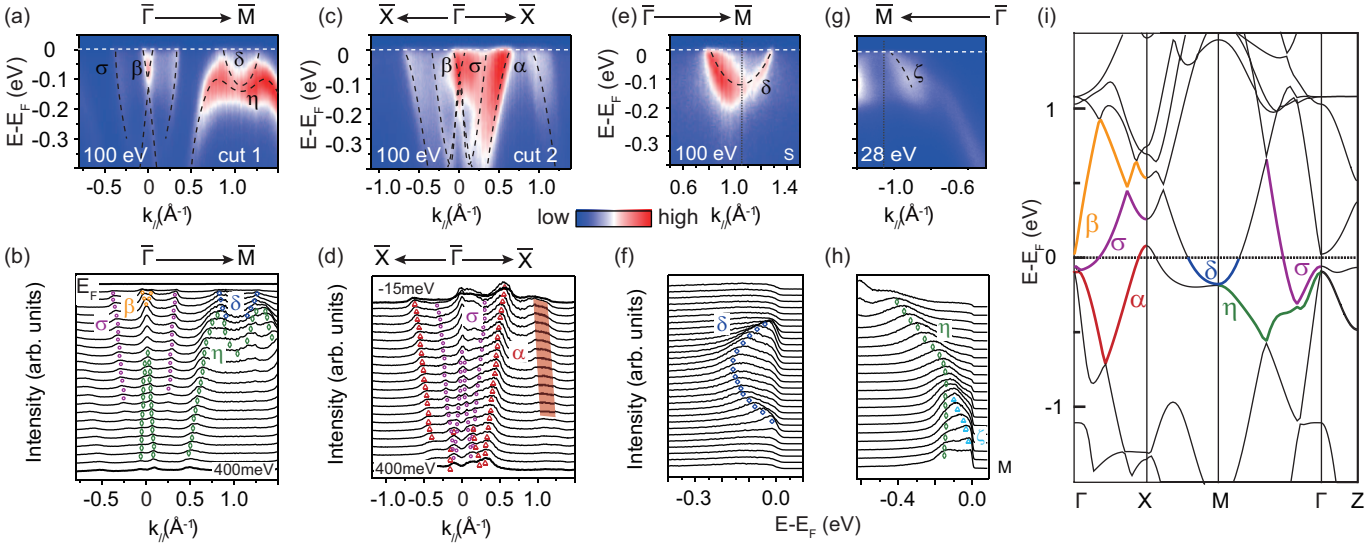

FIG. 3: (Color online) (a), (b) Photomission intensity and the corresponding MDCs taken with circularly polarized 100 eV photons along cut 1 marked in Fig. 2(d), respectively. The band dispersion is determined based on the MDCs and sketched onto the intensity plot. (c), (d) The same as panel (a) and (b), but taken along cut 2 marked in Fig. 2(d). (e), (f) Photomission intensity and the corresponding energy distribution curves (EDCs) near $\overline{M}$ along the $\overline{\Gamma}-\overline{M}$ direction, taken with 100 eV photons under s-polarization. (g), (h) The same as panels (e) and (f), respectively, but taken with circularly polarized 28 eV photons. (i) The calculated band structure of $BaTi_2Sb_2O$ taken from Ref. 15. Data were taken at 16 K at the SLS.

method with a modulation frequency of 973 Hz. The typical modulation amplitude (ΔV) was 5 mV.

III. 3D BAND STRUCTURE

Figures 2(a) - (c) show the photoemission intensity map of $Ba_{0.95}Na_{0.05}Ti_2Sb_2O$ measured with 100 eV photons at 16 K and 28 eV photons at 6 K, respectively, well into the density wave state. Combining these results, we obtained the Fermi surface in the projected two-dimensional BZ, as sketched in Fig. 2(d). The Fermi surface contains a small square-shaped electron pocket β (and a cross-shaped electron pocket β') together with a square-shaped intensity indicated as σ around the BZ center $\overline{\Gamma}$, a diamond-shaped hole pocket α together with a circular hole pocket α' around the BZ boundary $\overline{X}$ and a square-shaped electron pocket δ together with a circular hole pocket ζ around the BZ corner $\overline{M}$. As will be discussed below, α and α'(β and β') are actually different sections of the same Fermi surface, which is a consequence of an ARPES experiment with limited k_z resolution on a band that is strongly dispersive along the k_z direction, consistent with the band calculations shown in Fig. 3(i). It is clear that there are many nested Fermi segments in this multiband electronic structure.

The band dispersions along the high symmetry directions $\overline{\Gamma}$-$\overline{M}$ and $\overline{\Gamma}$-$\overline{X}$ in the projected two dimensional BZ are shown in Figs. 3(a) and (c), respectively, together with their corresponding momentum distribution curves (MDCs) shown in Figs. 3(b) and (d). Around $\overline{\Gamma}$, there is a V-shaped β band, and a W-shaped σ band along both directions. The α band is also W-shaped and crosses the Fermi level (E_F) along the $\overline{\Gamma}$-$\overline{X}$ direction, but not along the $\overline{\Gamma}$-$\overline{M}$ direction, since it contributes a Fermi pocket surrounding $\overline{X}$. Near $\overline{M}$, there is a M-shaped band below E_F, which is assigned as η. In particular, another weak feature near E_F in Fig. 3(a) is more clear in the data taken with linearly polarized light (s-polarization, as explained below) in Figs. 3(e) and (f), which is the parabolic δ band. Another band (ζ) becomes visible in the 28 eV data, as indicated in Figs. 3(g) and (h).

The corresponding parts of most of the observed bands can be found in the calculations reproduced in Fig. 3(i)[15], as indicated by the thickened curves and lables. For example, the electron-like δ band and the η band beneath it can be easily identified in the calculated band structure. However, there are also some discrepancies. For instance, the hole-like ζ band does not exist in the calculations; its origin is yet to be determined. Similarly, the dispersion of σ is not W-shaped along $\overline{\Gamma}$-$\overline{X}$ in the calculations, which might be caused by the inaccuracy in relative energy positions of various bands and additional hybridizations in the material. The comparison between the experimental and calculated bandwidths of η along several momentum cuts gives a renormalization factor of 1.0. Moreover, the band mass of the calculated δ aound M is 1.01 m_e, while the measured one is 1.31 m_e. All these results indicate that $Ba_{0.95}Na_{0.05}Ti_2Sb_2O$ is a weakly correlated material. We also note based on the calculations that α and η are in fact different sectors of one band, and the same holds true for δ and β.

To further explore the k_z dependence of the electronic structure of $Ba_{0.95}Na_{0.05}Ti_2Sb_2O$, we conducted a photon energy dependent ARPES experiment. The exploited photon energies range from 92 eV to 140 eV, covering more than one whole BZ along the k_z direction, as indicated in Fig. 4(a). The η

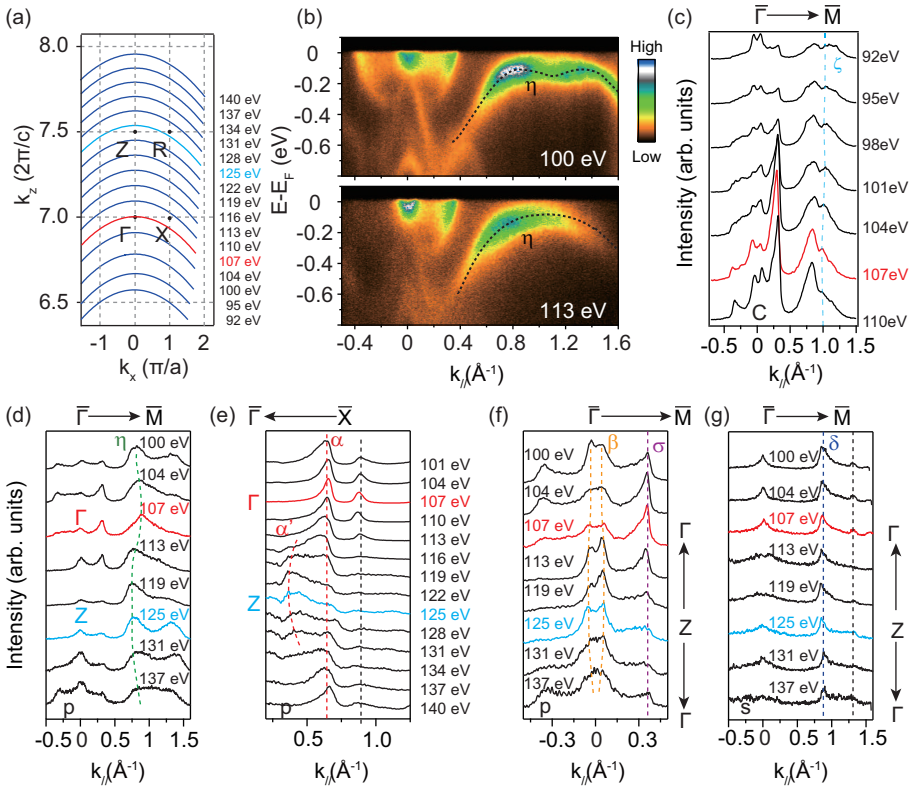

FIG. 4: (Color online) (a) Sketch of the BZs in Γ-*X*-*Z*-*R* plane. The corresponding positions for different photon energies are indicated, which are obtained using the fitted inner potential of 11 eV. (b) Top: photoemission intensity along Γ-*M* direction measured with 100 eV photons under *p*-polarization. Bottom: photoemission intensity along Γ-*M* direction measured with 113 eV photons under *p*-polarization. (c) The photon-energy dependence of the MDCs over [E_F-15 meV, E_F+5 meV]along the Γ-*M* direction. (d) MDCs at 100 meV below E_F as a function of photon energy. (e)-(g) MDCs at E_F as a function of photon energy, showing the dispersion of α, β, σ and δ along the k_z direction. The dashed lines in panel (c)-(g) are indications of the bands along k_z. Data were taken at the SLS except for data of panel (c), which was taken at the DLS.

band around M exhibits an obvious k_z dependence, as shown in Fig. 4(b) under two typical photon energies. The dispersion taken with 113 eV photons is parabolic, while it becomes "M"-like in data taken with 100 eV photons. Based on this obvious change in the η band, we plot the MDCs at 100 meV below E_F in Fig. 4(d). To match the periodic behavior of the η band along k_z , a 11 eV inner potential is choosen, and consequently Γ and *Z* can be determined to correspond to the photon energies of about 107 eV and 125 eV, respectively.

The k_z dispersions of all the bands that crosss E_F (α/α', β, σ and δ) are plotted in Figs. 4(c)- 4(g). For the α/α' band in Fig. 4(e), the MDC of α is quite sharp at the Γ point (107 eV), and becomes quite broad around the Z point (125 eV), then back to a sharp peak around Γ (140 eV) in the next BZ. This variation of the broadening of the α band matches the period of the BZ well. In the region where the peak of α band becomes broad, there are intensities of α' besides those of α. The existing both α and α' bands are in contrast with the calculations, where there is only one band around *X* [Fig. 3(i)]. However, because α exhibits strong k_z dependence, this can be understood by considering the poor k_z resolution of our photoemission experiment. That is, the α and α' bands actually originate from the same band with a strong k_z dependence, thus the projection of features at other k_z results in the coexisting α and α' bands across the entire k_z range [16]. This holds true for β and β' bands (data of β' bands were not showed). Although α and η show strong 3D nature, other bands are more 2D-like. ζ bands [Fig. 4(c)] show little k_z dependence while almost no k_z dependence can be detected for the σ [Fig. 4(f)] and δ bands [Fig. 4(g)]. The quasi-2D nature of these bands is consistent with the theoretical calculations of $BaTi_2Sb_2O$.

IV. ORBITAL CHARACTERS OF THE BANDS NEAR E_F

In both the calculations and our ARPES data, it is clear that $Ba_{0.95}Na_{0.05}Ti_2Sb_2O$ is a multiband system. Its electronic configuration is $3d^1$ for the Ti^{3+} ion, and multiple orbitals would participate in the low energy electronic structure. To further demonstrate the orbital characters of the bands, we have conducted polarization dependent ARPES experiments. The geometry of the photoemission experiment setup is shown in Fig. 5(a), where the path of the incident photon beam and the sample surface normal define the mirror plane. The *p* and *s* polarization of the light and the k_x and k_y directions of the sample are indicated in Fig. 5(a). With this experimental setup, the even (odd) *d* orbitals illustrated in Fig. 5(b) should be visible in *p* (*s*) geometry [17].

Figures 5(c)-(d) show the high symmetric photoemission intensity along the Γ-*M*, Γ-*X* directions under *p* and *s* polarizations, respectively. As summarized in Table I, the observed polarization dependence generally agrees with the calculated orbital characters of various bands [9]. More specifically, one finds that the σ band only shows up under *p* geometry along the Γ-*M* direction, indicating that it is composed of even orbitals in this direction [see Fig. 5(c)], which is consistent with the corresponding calculations. There is some residual intensity of the β band in Fig. 5(c), which might be caused by poor k_z resolution. Similarly, the projections of σ from other k_z's

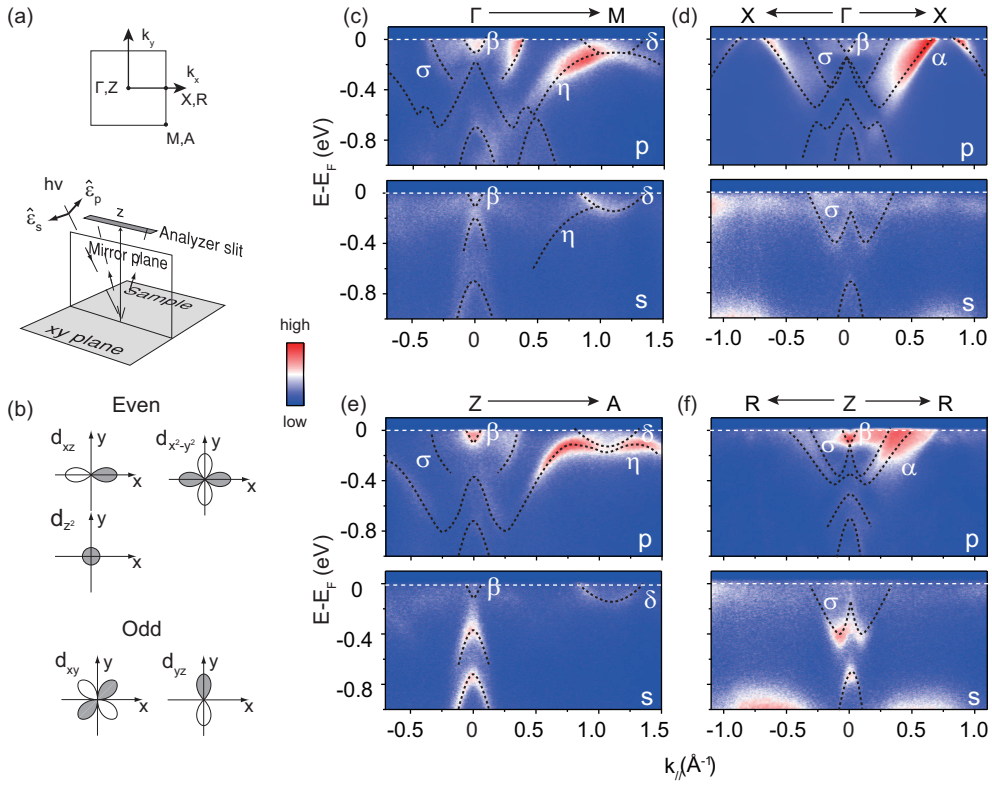

FIG. 5: (Color online) (a) Top: 2D projected BZ. The high symmetry points are indicated together with the defined k_x and k_y. Bottom: Experimental setup for polarization-dependent ARPES. For a p (or s) experimental geometry, the electric field direction of the incident photons is parallel (or perpendicular) to the mirror plane defined by the analyzer slit and the sample surface normal. (b) Illustration of the spatial symmetry of the 3d orbitals with respect to the mirror plane formed by the xz plane[20]. (c) Photoemission intensity measured along the Γ-M direction with p-polarized and s-polarized 107 eV photons, respectively. The dispersions of the bands are indicated by the dashed lines. (d) The same as panel (c), but taken along X-Γ-X directions. (e) Photoemission intensity measured along the Z-A direction with p-polarized and s-polarized 125 eV photons, respectively. (f) The same as pannel (e), but taken along R-Z-R direction. Data were taken at 16 K at the SLS.

broaden its feature along the Γ-X direction in the p geometry. The δ band around M is enhanced in s geometry than in the p geometry. Thus, the δ band should be composed primarily of a mixture of d_{xy} and/or d_{yz} orbitals, while the calculations show that it is mainly contributed by d_{xy}. Around the X point, the α band can only be observed under p geometry, which is again consistent with the calculated d_{z^2} and $d_{x^2-y^2}$ orbital characters.

In Figs. 5(e)- 5(f), we present the polarization dependent photoemission intensity along the Z-A and Z-R directions. The various bands here show almost the same polarization dependence as along Γ-M and Γ-X directions, respectively. As summarized in Table I, the calculated orbital characters in the Z plane are also largely the same as those in the Γ plane, and they generally explain the observed polarization dependence.

One also finds that there are some discrepancies between the data and the calculations. In particular, σ band is clearly present in the data taken with s-polarization along the Z-R direction, however, there is no corresponding odd orbitals in the calculations. Also the α band, exhibiting odd orbital character according to calculation, is found in our p-polarized experimental data instead along the Z-R direction. These need further investigations, including further analysis using Bloch wavefunctions [17]. Nevertheless, the general agreement between the experiment and calculations suggests that the low-lying electronic bands, which are responsible for both the CDW and superconductivity, arise mainly from the Ti 3d states.

V. CHARGE DENSITY WAVE STATE

We now search for the electronic structure signature of the CDW state of $Ba_{0.95}Na_{0.05}Ti_2Sb_2O$. For a conventional CDW ground state, the scattering of electrons between the nested Fermi surfaces effectively drives the system into an ordered ground state. Consequently, a CDW gap opens at E_F. For example, gap opening at the Fermi surface has been reported in 1T-structured TaS_2 [18]. However, for 2H-structured TaS_2, there is no CDW gap at the Fermi surface, instead, partial gap opening has been observed over the Fermi patches. The CDW vector match is fulfilled through participation of all the states in the Fermi patches [18]. This behavior has been observed in the density wave state of $BaTi_2As_2O$ as well [6]. Furthermore, it has been shown in $NbSe_2$ that the collective contribution of the weakly occupied states can dominate the CDW formation [19]. Therefore, one needs to study the temperature depen-

TABLE I: Comparison between the polarization-dependent APRES measurements in p and s geometries, and the calculated orbital characters of the bands along four high symmetry directions [15].

	Experiment				Calculation			
	Γ-M		Γ-X		Γ-M		Γ-X	
	p	s	p	s	p	s	p	s
α			√				d_{z^2}, $d_{x^2-y^2}$	
β	√	*weak*	√		d_{z^2}		d_{z^2}	
σ	√		√	√	d_{z^2}, d_{xy}			d_{xy}
δ	*weak*	√			d_{z^2}, d_{xy}	$d_{x^2-y^2}$		
η	√	√			d_{z^2}, d_{xy}	$d_{x^2-y^2}$		
	Experiment				Calculation			
	Z-A		Z-R		Z-A		Z-R	
	p	s	p	s	p	s	p	s
α			√					d_{xy}
β	√	*weak*	√		d_{xz}, d_{yz}	d_{xz}, d_{yz}	d_{xz}	
σ	√		√	√	d_{z^2}		d_{z^2}	
δ	*weak*	√			d_{z^2}, d_{xy}	$d_{x^2-y^2}$		
η	√				d_{z^2}, d_{xy}	$d_{x^2-y^2}$		

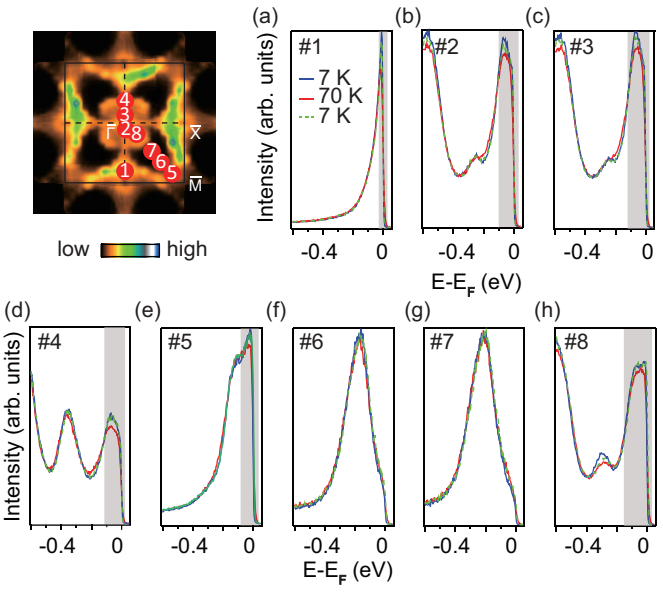

FIG. 6: (Color online) (a)-(h) Temperature dependence of the EDCs taken at the momenta 1-8 as marked in inset. To compensate for thermal broadening effects, the 70 K data have been divided by the resolution convoluted Fermi-Dirac functions and then multiplied by that of 7 K. The data were taken in the sequence of 7 K (blue curves), 70 K (red curves), and then the temperature was cycled back to 7 K (dashed curves). Data were taken at the SSRL. The shades highlight regions with noticeble temperature dependneces.

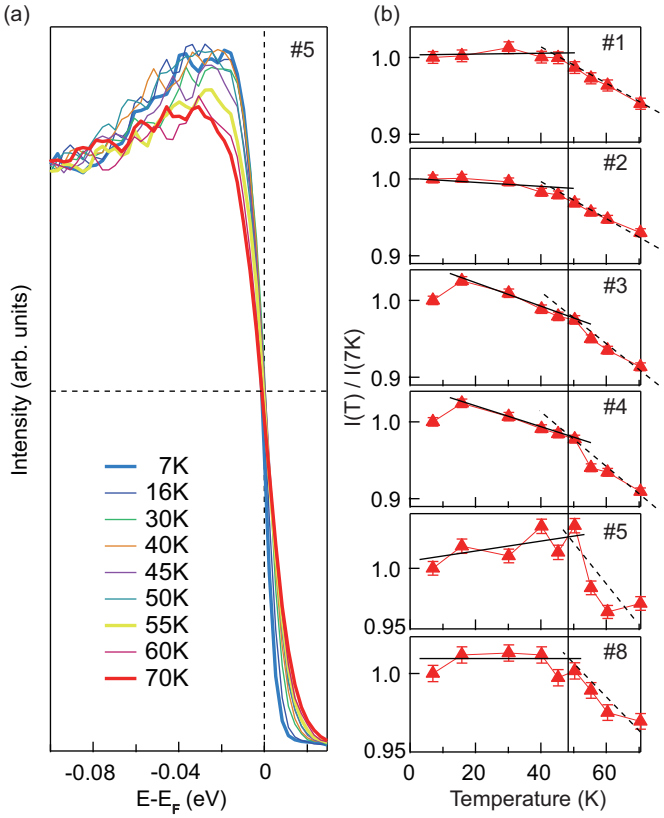

FIG. 7: (Color online) More detailed temperature dependence for the data in Fig. 6, for momentum positions as labelled in the inset of Fig. 6. (a) Temperature dependence of EDCs at position 5. To compensate for thermal broadening near E_F, the spectra were divided by the resolution convoluted Fermi-Dirac function at their corresponding temperatures and then multiplied by that of 7 K. (b) The temperature dependence of the spectral intensities integrated over the shaded regions of Figs. 6(a)-(e) and (h) for momentum positions 1-5, and 8, respectively, where the spectra exhibit obvious temperature dependences.

dence of the electronic structure over the entire BZ or at least over the Fermi patches.

Figure 6 shows 7 K and 70 K photoemission spectra of $Ba_{0.95}Na_{0.05}Ti_2Sb_2O$ taken at different momenta along the $\overline{\Gamma}$-$\overline{X}$ and $\overline{\Gamma}$-$\overline{M}$ directions, respectively. Instead of a gap opening or a spectral weight suppression, there is just some minor enhancement of the spectral weight in the 7 K spectra. As highlighted by the shaded regions, the spectral weight enhancement occurs in the energy range of 30∼110 meV below

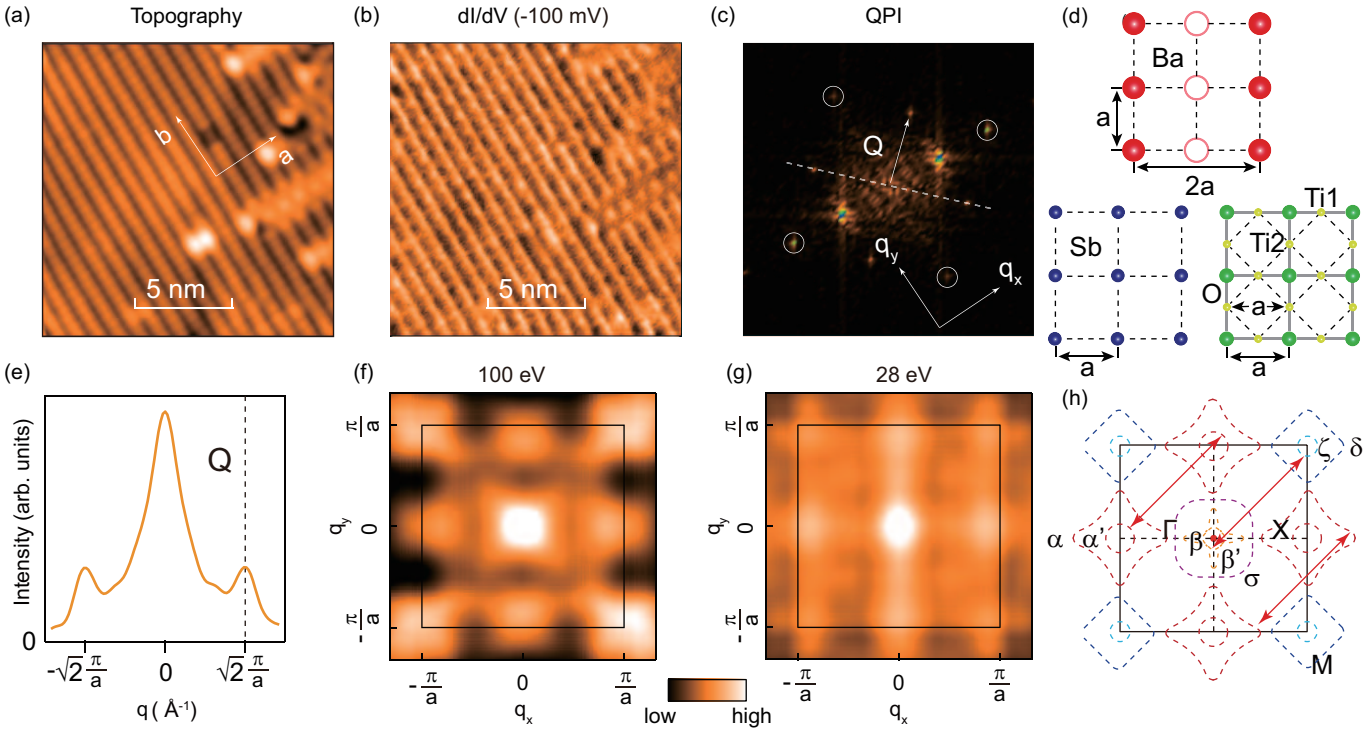

FIG. 8: (Color online) (a) STM topography image of the *in − situ* cleaved (001) surface of $Ba_{0.95}Na_{0.05}Ti_2Sb_2O$ measured at 4.5 K (V_{bias}=-100 mV, I=100 pA). Scanned areas:15 nm×15 nm. (b) The differential conductance map measured in the same area as in panel (a), taken with the bias voltage of -100 mV. (c) The corresponding Fourier transform of panel (b), which gives the quasiparticle interference (QPI) plot. The four circled points are the lattice Bragg spots. (d) A schematic shows different layers of the sample. (e) Intensity cut of the QPI plot along the (π, π) direction, as shown by the dashed line in panel (c). Q is (π, π). (f), (g) Two dimensional autocorrelation maps at E_F [joint density-of-states $C(\vec{q}, 0)$] for ARPES intensity distributions taken at 100 eV and 28 eV, respectively. (h) Schematic of the wave vector (π, π) on the Fermi surface.

E_F. The agreement of the 7 K data before and after thermal cycling indicates the observed spectral changes are intrinsic. For simplicity, we do not show the EDCs taken at the temperatures in between 7 K and 70 K for these momenta.

To further study the detailed temperature evolution, Fig. 7(a) shows the detailed temperature dependence of the photoemission spectrum taken at momentum position 5. With decreasing temperature from 70 K, the spectrum first exhibits a sizable enhancement and then saturates at low temperatures, while a leading-edge gap is always absent. The integrated intensity within [E_F-80 meV, E_F+30 meV] is shown in Fig. 7(b) as a function of temperature. Similar behavior has also been observed at various other momentum positions as shown in Fig. 7(b). For some momenta, there is no saturation behavior at low temperatures, but as shown by the two lines, there is a clear change of slope around the density wave transition temperature. With decreasing temperature, the intensity increases much slower below T_{DW} than above it. Moreover, we note that there is an additional suppression at the lowest temperature at several momenta. The enhancement above the density wave transition temperature is unlikely due to the density wave formation. As an alternative, strong electron-phonon interactions can induce similar temperature dependence [6]. The slope decrease below T_{DW} suggests that the density wave formation may be responsible for suppressing the spectral weight there. Similar behavior has been observed in $BaTi_2As_2O$, that is, an additional spectral weight suppression occurs at the Fermi patches below its density wave transition temperature beyond the continuous spectral evolution with temperature over an energy range of 200~500 meV [6], which is also manifested as a slope change for the integrated spectral weight. The transition temperature of $Ba_{0.95}Na_{0.05}Ti_2Sb_2O$ is about a quarter of that of $BaTi_2As_2O$ (200 K), and the energy scale for the lineshape change in the latter compound is over an energy range of 30~110 meV, also about a similar fraction of that of the former compound. This intriguing scaling behavior of these two systems suggests that their density waves share similar nature, although the density wave in $Ba_{0.95}Na_{0.05}Ti_2Sb_2O$ is much weaker. We note that these energy scales are much larger than the mean field gap size of a density wave, which is about $\Delta \sim 1.76\, k_B T_{DW} \approx 7$ meV for $Ba_{0.95}Na_{0.05}Ti_2Sb_2O$. However, such a relatively large energy scale has been commonly observed in systems with strong electron-phonon interactions [18].

To reveal the nature of the density wave in $Ba_{0.95}Na_{0.05}Ti_2Sb_2O$, we have further conducted STM measurements. Figure 8(a) shows a typical topographical image of a 15 nm × 15 nm region measured at 4.5 K. The cleaved surface is expected to be the Ba-terminated surface, where there forms a strong 2×1 reconstruction of

Ba atoms. The differential conductance (dI/dV) mapping at V_b=-100 mV, which reflects the spatial distribution of local density of states (LDOS), is plotted in Fig. 8(b). One can see that a strong 2×1 reconstruction exists in both topographic and dI/dV mappings of the Ba atoms, since about half of the Ba atoms are lost during the cleavage. This reconstruction is so strong that it hinders the observation of other weak modulations.

In order to reveal all the proper existing structural and electronic orders, the Fourier transform of the differential conductance map is shown in Fig. 8(c). The two points with strongest intensities represent the 2×1 reconstruction of Ba atoms, and the four circle-highlighted points are from the periodicity of the atomic structure. Fig. 8(d) sketches the periodicity of Ba atoms in the first layer, Sb atoms in the second layer, and O atoms in the third layer. One should note that there are four additional points at 45° to q_x or q_y [Fig. 8(c)], marked by Q. The wavevector of this periodicity is (π, π), which is beyond the crystalline Bragg spots. This thus should correspond to the long-sought CDW formation.

Furthermore, to further demonstrate the contribution to the CDW instability, we calculated the weighted joint density-of-states $C(\vec{q},0)$ of the photoemission intensity at E_F, which has proven effective at identifying Fermi surface instabilities [18].The formula is

$$C(\vec{q},\omega) \equiv \int M(\vec{k}, \vec{k}+\vec{q})A(\vec{k}, \omega)A(\vec{k}+\vec{q}, \omega)d\vec{k},$$

where

$$M = \begin{cases} 1 & \vec{k}+\vec{q}, \vec{k} \in \text{weight-suppressed region} \\ 0 & \text{otherwise} \end{cases} \quad (1)$$

Ideally, one needs to integrate over the entire three dimensional BZ, however, due to experimental limitations, only several 2D maps can be taken. The resulting $C(\vec{q},0)$ calculated for the photoemission intensity maps in Figs. 2(a) and 2(b) are shown in Figs. 8(f) and 8(g), respectively. A strong peak is observed at (π, π) in Fig. 8(f). This is consistent with the (π, π) wavevector found in the STM results, and the theoretical calculations [10]. Therefore the Fermi surface instability is likely the driving force of the CDW, which is contributed largely by the nested Fermi sectors as indicated in Fig. 8(e). We note that many instabilities at other $\vec{q}$s coexist with the (π, π)—for example, there is also a weak peak near (π, 0). However, in the competition amongst various CDW instabilities, the fastest-growing instability will cause the corresponding phonon-softening, and induce static charge order.

VI. DISCUSSIONS AND CONCLUSIONS

In conclusion, we resolved low energy electronic structure of the superconducting material $Ba_{0.95}Na_{0.05}Ti_2Sb_2O$, which is dominated by Ti $d_{x^2-y^2}$, d_{xy} and d_{z^2} orbitals. We find that correlation effects are weak in this system.

We have found the first direct evidence of CDW order in this material with STM, and the ordering wavevector is (π, π). The strength of the CDW is weak, so that its usual manifestation, namely band folding or a gap or spectral weight suppression, cannot be resolved in the photoemission spectra. Instead, we observe a spectral weight enhancement with decreasing temperature, which might be induced by strong electron phonon interactions. The rate of this spectral weight enhancement at low temperatures is reduced or diminished in the CDW state, which suggests that CDW may open a partial gap, but it is compensated by the overall spectral weight enhancement. The observed Fermi surface is well nested along the (π, π) direction, consistent with the CDW wavevector found by STM. Moreover, the autocorrelation of the photoemission intensity, an indication of the charge instability, also exhibits a peak at (π, π). This suggests that the Fermi surface instability is the driving force behind the CDW in $Ba_{0.95}Na_{0.05}Ti_2Sb_2O$.

The observed weak correlation and the CDW suggest that electron-phonon interactions, rather than spin fluctuations, underpin superconductivity in $Ba_{0.95}Na_{0.05}Ti_2Sb_2O$. On the other hand, compared with other titanium pnictide oxides, the CDW affects the electronic structure of $Ba_{0.95}Na_{0.05}Ti_2Sb_2O$ much more weakly. In fact, the spectral intensity at the Fermi energy is not reduced at low temperatures due to an underlying global enhancement. Since the CDW is expected to compete with superconductivity, the weak CDW here might be the reason why superconductivity found so far only in $Ba_{1-x}Na_xTi_2Sb_2O$ and not in the other other titanium pnictide oxides. One may expect superconductivity when CDW order is further reduced in other systems by certain means. Our results pave the way for further understanding of the superconductivity and the CDW in this class of systems.

Acknowledgement: We thank Dr. M. Shi and Dr. N. Xu at SLS, Dr. D. H. Lu at SSRL, and Dr. P. Dudin, Dr. T. Kim and Dr. M. Hoesch at DLS for experimental help, and Dr. D. Peets for helping with the text. This work is supported in part by the National Science Foundation of China and National Basic Research Program of China (973 Program) under grant Nos. 2012CB921402, and Science and Technology Committee of Shanghai Municipal. SSRL is operated by the U. S. DOE Office of Basic Energy Science.

[1] A. R. Moodenbaugh, Y. Xu, M. Suenaga, T. J. Folkerts and R. N. Shelton, Phys. Rev. B **38**, 4596 (1988).

[2] H. Luetkens, H.-H. Klauss, M. Kraken, F. J. Litterst, T. Dell-

mann, R. Klingeler, C. Hess, R. Khasanov, A. Amato, C. Baines, M. Kosmala, O. J. Schumann, M. Braden, J. Hamann-Borrero, N. Leps, A. Kondrat, G. Behr, J. Werner and B. Buchner, Nat. Mater. **8**, 305 (2009).

[3] E. Morosan, H. W. Zandbergen, B. S. Dennis, J. W. G. Bos, Y. Onose, T. Klimczuk, A. P. Ramirez, N. P. Ong and R. J. Cava, Nat. Phys. **2**, 544 (2006).

[4] T. C. Ozawa and S. M. Kauzlarich, Sci. Technol. Adv. Mater. **9**, 033003 (2008).

[5] X. F. Wang, Y. J. Yan, J. J. Yin, Q. J. Li, N. Xu and X. H. Chen, J. Phys.: Condens. Matter **22**, 075702 (2010).

[6] H. C. Xu, M. Xu, R. Peng, Y. Zhang, Q. Q. Ge, F. Qin, M. Xia, J. J. Ying, X. H. Chen, X. L. Yu, L. J. Zou, M. Arita, K. Shimada, M. Taniguchi, D. H. Lu, B. P. Xie and D. L. Feng, Phys. Rev. B **89**, 155108 (2014).

[7] T. Yajima, K. Nakano, F. Takeiri, T. Ono, Y. Hosokoshi, Y. Matsushita, J. Hester, Y. Kobayashi and H. Kageyama, J. Phys. Soc. Japan **81**, 103706 (2012).

[8] P. Doan, M. Gooch, Z. J. Tang, B. Lorenz, A. Moller, J. Tapp, P. C. W. Chu and A. M. Guloy, J. Am. Chem. Soc. **134**, 16520 (2012).

[9] D. J. Singh, N. J. Phys. **14** 123003 (2012).

[10] A. Subedi, Phys. Rev. B **87**, 054506 (2013).

[11] F. vonRohr, A. Schilling, R. Nesper, C. Baines and M. Bendele, Phys. Rev. B **88**, 140501 (2013).

[12] S. Kitagawa, K. Ishida, K. Nakano, T. Yajima and H. Kageyama, Phys. Rev. B **87**, 060510 (2013).

[13] M. Gooch, P. Doan, Z. J. Tang, B. Lorenz, A. M. Guloy and P. C. W. Chu, Phys. Rev. B **88**, 064510 (2013).

[14] S. Y. Tan, J. Jiang, Z. R. Ye, X. H. Niu, Y. Song, C. L. Zhang, P. C. Dai, B. P. Xie, X. C. Lai and D. L. Feng, Sci. Rep. **5**, 9515 (2015)

[15] G. T. Wang, H. P. Zhang, L. Zhang, and C. Liu, Journal of Apply Physics **113**, 243904 (2013).

[16] Z. R. Ye, Y. Zhang, F. Chen, M. Xu, J. Jiang, X. H. Niu, C. H. P. Wen, L. Y. Xing, X. C. Wang, C. Q. Jin, B. P. Xie, and D. L. Feng, Phys. Rev. X **4**, 031041 (2014).

[17] For practical purposes, atomic orbitals, instead of Bloch wavefunctions, are used for the symmetry analysis, but they usually give the same results.

[18] D. W. Shen, B. P. Xie, J. F. Zhao, L. X. Yang, L. Fang, J. Shi, R. H. He, D. H. Lu, H. H. Wen and D. L. Feng, Phys. Rev. Lett. **99**, 216404 (2007).

[19] D. W. Shen, Y. Zhang, L. X. Yang, J. Wei, H. W. Ou, J. K. Dong, B. P. Xie, C. He, J. F. Zhao, B. Zhou, M. Arita, K. Shimada, H. Namatame, M. Taniguchi, J. Shi and D. L. Feng, Phys. Rev. Lett. **101**, 226406 (2008).

[20] Y. Zhang, F. Chen, C. He, B. Zhou, B. P. Xie, C. Fang, W. F. Tsai, X. H. Chen, H. Hayashi, J.Jiang, H. Iwasawa, K. Shimada, H. Namatame, M. Taniguchi, J. P. Hu, and D. L. Feng, Phys. Rev. B **83**, 054510 (2011).